

A comprehensive study of non-linear air damping and “pull-in” effects on the electrostatic energy harvesters

Xingke Guo^a, Yulong Zhang^a, Kangqi Fan^b, Chengkuo Lee^c, Fei Wang^{a,*}

^a School of Microelectronics, Southern University of Science and Technology, Shenzhen 518055, China

^b School of Mechano-Electronic Engineering, Xidian University, Xi'an 710071, China

^c Department of Electrical & Computer Engineering, National University of Singapore, Singapore 117576, Singapore

ARTICLE INFO

Keywords:

Energy harvester
Electrostatic
Air damping
Pull-in effect
Non-linearity

ABSTRACT

In this paper, a new comprehensive model is presented to optimize the design of vibration based electrostatic energy harvester working in standard atmosphere. This model considers the non-linear air damping force induced by the movement of proof mass as well as the “pull-in” effect from the electrostatic force. Important parameters such as the height of stoppers on the bottom plate, the initial gap between the bottom plate and proof mass and the surface potential of the electret layer have been investigated. With the microelectromechanical system (MEMS) technology, a series of energy harvesters have been fabricated with various parameters. The measurements of devices show excellent agreement with the simulations. For the first time, the “pull-in” phenomenon has been observed during the harvesting test as our expectation. The model provides a promising optimization route for the electrostatic energy harvester with broad bandwidth, decent power output while avoiding the “pull-in” effect.

1. Introduction

With the fast development of micro wireless sensors and communication technology, wireless sensor networks (WSN) and internet of things (IoT) have been emerging with wide applications, where traditional power supply of battery encounters the limitation of lifetime and the challenge of replacement for large scale networks [1–3]. Energy harvesting technology may provide supplementary power with sustainable and renewable energy from vibration energy [4–7], thermal energy [8,9] and flow energy [10,11], etc. For instance, vibration-based energy harvesters have been developed in self-powered systems for bridge health monitoring and wireless temperature sensing [12,13], which have shown promising performance to replace the batteries.

Three principles such as electromagnetic [14–16], piezoelectric [17–19] and electrostatic [20–27] methods have been usually used for the energy conversion from ambient vibration sources to electricity. Among these approaches, the electrostatic vibration-based energy harvester (e-VEH) is more competitive in compact size, energy density and compatibility to micro-electro-mechanical system (MEMS) technology. A linear mass-beam system is typically used with variable capacitor structures where a bias voltage or pre-charged electret layer is applied. When the mass vibrates along with the vibration source, the changing of the overlapping area or the distance between the two plates

will lead to a capacitance variation; and therefore, electric current can be generated [4]. A prototype of MEMS e-VEH device was fabricated by Y. Suzuki in 2010, which provided a total power output of 1.0 μW at an in-plane acceleration of 2 g with 63 Hz [20]. And a fully packaged MEMS e-VEH was developed with a four-wafer stack to harvest energy from out-of-the-plane vibration source [21]. The overall size of the device was only about 1.1 cm \times 1.3 cm, and a power output of 0.15 μW was achieved at an acceleration amplitude of 1 g with a frequency of 96 Hz. A device with maximum output power as 20.7 μW at 110 Hz and 2 g with device size as 1 cm \times 4 cm was achieved by Lee [25]. In 2011, a maximum output power of 50 μW was obtained from an energy harvester with out-of-plane cantilever [26]. Besides, a non-linear e-VEH with maximum output as 4.5 μW and active chip size as 1 cm \times 1.2 cm which can harvest energy from 10 Hz to up to 162 Hz was put forward by Y. Lu et al. [27].

For all the three types of harvesters with linear mass-beam system, it is a common challenge to improve the bandwidth of the device for harvesting the vibration energy with random frequency spectrum. Therefore, nonlinearity has been introduced and studied widely for them. For the electromagnetic and the piezoelectric harvesters, to increase their operational bandwidth, multi-well potentials with bi-stable or tri-stable resonant systems has been realized with buckling beam or external magnets [28–33]. Recently, for e-VEHs, bi-stable spring and

* Corresponding author.

E-mail address: wangf@sustech.edu.cn (F. Wang).

<https://doi.org/10.1016/j.enconman.2019.112264>

Received 7 June 2019; Received in revised form 4 October 2019; Accepted 6 November 2019

Available online 14 November 2019

0196-8904/ © 2019 Elsevier Ltd. All rights reserved.

Nomenclature

Symbol Parameters

A	area of the damping film
c	coefficient of damping force
C_{par}	parasitic capacitor
$C(t)$	capacitance between the top electrode and bottom electrode
C_{air}	capacitance of the air gap
C_{ele}	capacitance of the electret
d_{ele}	electret thickness
E	electrostatic energy
f	frequency
F_{air}	air damping force
F_{ele}	electrostatic force
F_{spring}	spring force
F_{bottom}	air damping caused by bottom surface
$F_{stopper}$	air damping caused by stoppers' surface
g	gravitational acceleration
h	instantaneous distance between two plates (the air film thickness)
h_0	initial distance between two plates
h_s	stopper height
H	silicon wafer thickness

k	equivalent stiffness of four silicon springs
l	the typical dimension of the plate (half of the side length for the square bottom plate of our device)
K	linear stiffness coefficient
L	silicon beams' length
m	proof mass
P	pressure
P_0	initial pressure
Q	induced charge
R	external load resistance
t	silicon beams' thickness
v	velocity of the proof mass
V_s	surface potential of the electret material
w	beam width
X	vertical displacement of the proof mass
Y	vertical displacement of the external ambient vibration source
μ	coefficient of viscosity (air)
ω	angular frequency of the applied sinusoidal vibration
ϵ	Excursion calculated through $(h_0-h)/h_0$
ϵ	the absolute dielectric permittivity.
σ	squeeze number
γ	the ratio of the plate length to the plate width
ρ	density of the gas (air)

mechanical collision have also been utilized for wideband energy harvesting [34,35]. Besides, through amplitude limitation of package cap and reducing air damping in vacuum chamber, both broad bandwidth and high normalized power density were successfully achieved [36]. For all the devices above, unfortunately, the nonlinearity of the air damping has been overlooked for a long time, simply because the air damping force is comparably smaller than the transduction force in the electromagnetic and piezoelectric harvesters. However, this air damping could be significant in e-VEHs, especially for the device with out-of-the-plane scheme, where the squeeze film damping force increases dramatically when the air gap decreases during vibration [37]. Therefore, a detailed study on the nonlinearity of the air damping force is necessary for the optimization of the harvester.

On the other hand, performances of electrostatic MEMS devices are also strictly limited to the “pull-in” effect, when the electrostatic force is larger than the spring force due to the small gap between the two electrodes. This effect will lead to severe instability to electrostatic MEMS devices. During the past decades, various models or methods have been developed to study this nonlinear phenomenon for electrostatic MEMS/NEMS devices [38]. For MEMS e-VEH, the electrostatic force could be large enough to induce the “pull-in” state, when the mass approaches to the counter electrode during the vibration. This “pull-in” phenomenon has never been observed in e-VEHs previously, while it also should be taken into consideration for the device design. In this paper, we have proposed the optimization of e-VEH device with the non-linear air damping force in gap-closing scheme. A comprehensive model has been built to study the influence of the initial gap, stopper height and surface potential to the air damping, the “pull-in” effect and the power output of the harvester. MEMS e-VEH devices were fabricated with IC-compatible process according to our design, demonstrating excellent agreement between the experiments and the simulations. As expected, we have observed the “pull-in” phenomenon during the energy harvesting process for the first time. The modeling in this work shows promising optimization route for the design of an e-VEH with broad bandwidth, decent power output while avoiding the risk of “pull-in” effect.

2. Theoretical analysis and simulation

The 3D-scheme and the 2D cross-section view of the e-VEH with out-of-plane gap-closing structure are shown in Fig. 1(a) and (b), respectively [39]. A few stoppers are designed either on the proof mass or on the bottom electrode to avoid the “pull-in” effect. As shown in Fig. 2, the electro-mechanical characteristic of the device is generally described by the equation below,

$$m(\ddot{Y} + \ddot{X}) + F_{spring} + mg + F_{air} + F_{ele} = 0 \quad (1)$$

where X and Y are the displacement of the proof mass and the external ambient vibration source. For our devices, the length of the four silicon

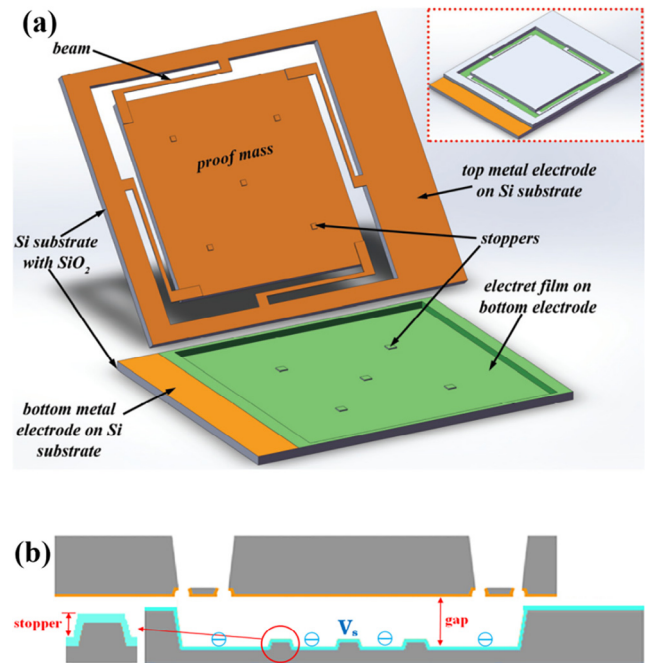


Fig. 1. (a) The 3D-scheme of the e-VEH; (b) The 2D-scheme of the bottom plate.

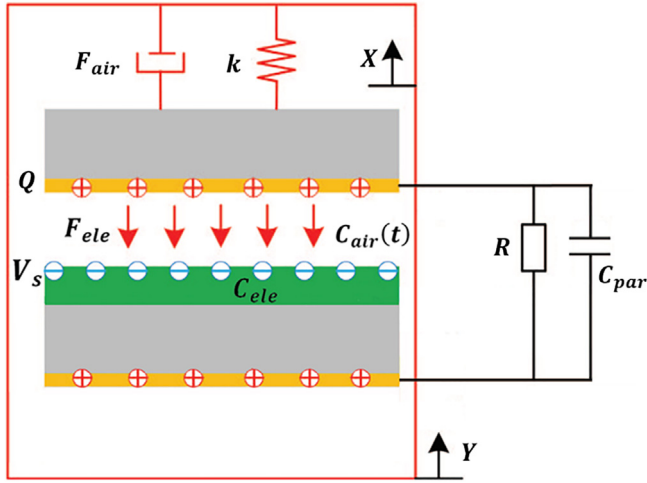


Fig. 2. The electro-mechanical model of the e-VEH.

springs is 8 mm while the maximum displacement of the proof mass ranges from 200 μm to 300 μm , so these springs won't exhibit non-linearity during vibration and the spring force is linearly proportional to the displacement of the proof mass:

$$F_{\text{spring}} = -kX \quad (2)$$

where k is the total equivalent stiffness of the four silicon springs.

2.1. Squeeze-film air damping force

2.1.1. Calculation

For our devices working at room temperature and atmosphere, the Knudsen number, which reveals the gas rarefaction calculated through the ratio of the mean molecular free path and the characteristic length scale is smaller than 0.001. In this regime, the gas can be classified as continuum flow with no slip at walls. Furthermore, we assume that the air film is isothermal, and the Reynolds' equation derived from Navier-Stokes equation in the situation can be written as [37]:

$$\frac{\partial}{\partial x} \left(P \frac{h^3}{\mu} \frac{\partial P}{\partial x} \right) + \frac{\partial}{\partial y} \left(P \frac{h^3}{\mu} \frac{\partial P}{\partial y} \right) = 12 \frac{\partial(h\rho)}{\partial y} \quad (3)$$

where x and y are the axes along the sides of the bottom plate and h is the distance between the two plates, or the thickness of the gas film. Meanwhile, the initial distance at the equilibrium position, h_0 , can be calculated through mechanical equilibrium equation in stationary situation:

$$F_{\text{spring}}(h_0) + mg + F_{\text{ele}}(h_0) = 0 \quad (4)$$

For devices with no stoppers, h can be assumed as uniform both in the x - and y - directions; therefore, the Reynolds' equation (Eq. (3)) could be simplified as [37]:

$$\frac{\partial}{\partial x} \left(P \frac{\partial P}{\partial x} \right) + \frac{\partial}{\partial y} \left(P \frac{\partial P}{\partial y} \right) = \frac{12\mu}{h^3} \frac{\partial(h\rho)}{\partial y} \quad (5)$$

Now another important factor, the squeeze number, σ , required to be considered. For the square air damping film, it is defined as:

$$\sigma = \frac{12\mu l^2 \omega}{P_0 h_0^2} \quad (6)$$

For this e-VEH device, the value of squeeze number versus h is shown in Fig. 3. It can be noticed that, when the distance between two plates is larger than 60 μm , the squeeze number is far smaller than 1 and the air flow can be considered as incompressible. Whereas, when the distance becomes smaller than 60 μm , the air compressibility cannot be further neglected.

At small squeeze number ($\sigma \ll 1$), the air damping force is only caused by the viscous damping and the fluid can be considered as incompressible. At finite squeeze number, the air flow will be limited and the movement of the proof mass will approach the circumstance like pressing a piston inside a closed container [40], in which situation the squeezed air film behaves more like a spring and the air damping force is the sum of the damping caused by the air compressibility and the damping caused by the viscosity. Through Fig. 3, we found that the squeeze number could be considered far smaller than one when the distance between two plates is larger than 60 μm . Thus, when applying a small external excitation, the minimum distance between two plates is larger than 60 μm ; therefore, the simplified Reynolds' equation could be solved by directly applying popular following boundary conditions to get the pressure distribution $P(x, y)$:

$$\begin{cases} P_{(x=\pm l)} = 0 \\ P_{(y=\pm l)} = 0 \end{cases} \quad (7)$$

And F_{air} can be calculated through the integration of the pressure with the area [37]:

$$\begin{aligned} F_{\text{air}} &= \int_{-l}^l \left(\int_{-l}^l (P(x, y) dx) \right) dy \\ &= -\frac{\mu(2l)^4}{h_0^3} v \left\{ 1 - \frac{192}{\pi^5} \sum_{n=1,3,5,\dots}^{\infty} \frac{1}{n^5} \tanh\left(\frac{n\pi}{2}\right) \right\} \\ &= -0.42 \cdot \frac{\mu(2l)^4}{h_0^3} \cdot v \quad (8) \\ &\equiv -c_0 v \quad (9) \end{aligned}$$

It could be noticed that, this force doesn't depend on the pressure (μ is considered as a constant for ideal gas at different pressures) for the reason we introduced at the beginning of this section, that we only considered the device working at room temperature and standard atmosphere in which Knudsen number is lower than 0.001 and the model was also built based on that. For devices working at low or high vacuum, the gas will show different characteristics and new models required to be built, like the slip length, the transitional flow and the free molecular flow.

Whereas, for our devices with out-of-plane motion, the above boundary conditions are not accurate when the film thickness is too large to be considered as significantly smaller than the device dimension. A modified boundary condition is required; therefore, the coefficient and the value of the damping force should be modified as [41],

$$c = c_0 \cdot \left(1 + \chi \frac{6\Lambda}{h_0} \right)^{-1} \cdot \left\{ 1 + 3\eta \left(\frac{h_0}{l} \right) + 3\zeta \left(\frac{h_0}{l} \right)^2 \right\} \quad (10)$$

$$F_{\text{air}} = -c \cdot v \quad (11)$$

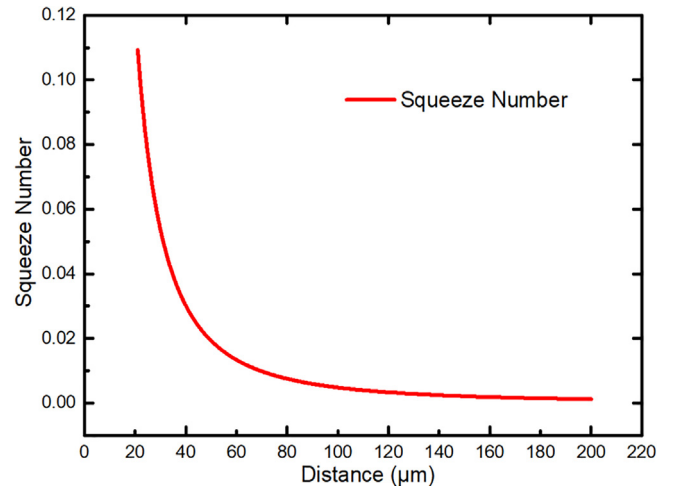


Fig. 3. The value of the squeeze number versus distance between the two plates.

where Λ is the slip length, which has the same order as the molecular mean free path, and χ , η and ζ are three coefficients depending on the ratio of the slip length to the film thickness. These coefficients values could be calculated as shown in [41]. For our device at room temperature and standard atmosphere, $\chi = 1$, $\eta = 0.634$ and $\zeta = 0.445$ are applied for the following analysis.

As we discussed previously, when the vibration amplitude is small and the minimum film thickness is larger than $60 \mu\text{m}$, the squeeze-film air damping force is proportional to the velocity of the proof mass. For a large external excitation, however, the distance between two plates could be smaller than $60 \mu\text{m}$, and the squeeze number might be close to one or even larger than one. If the motion of the proof mass is a sinusoidal vibration with excursion ϵ , which is given by the ratio of vibration amplitude to the initial gap (initial film thickness), i.e., ϵ is equal to $(h_0 - h)/h_0$. According to the derivation in [42], the air damping force should be calculated as:

$$F_{air} = -c \cdot v - K \cdot (h_0 - h) \quad (12)$$

where K is the linear stiffness coefficient calculated through:

$$K = \frac{AP_0\sigma^2 b_1}{h_0} \cdot \frac{1 + 3\epsilon^2 + \frac{3}{8}\epsilon^4}{(1 - \epsilon^2)^{\frac{9}{2}}} \quad (13)$$

and b_1 is a coefficient relative to γ , the ratio of the plate length to the plate width:

$$b_1 = \sum_{n=1}^{\infty} \frac{1}{\alpha^6} \left[3 \cdot \left(1 - \frac{\tanh(\alpha\gamma)}{\alpha\gamma} \right) - \tanh^2 \alpha\gamma \right] \\ \alpha = \frac{2n-1}{2} \pi \quad (14)$$

Besides, in this condition, the coefficient of the damping force also needs to be further modified due to the increasing damping,

$$c_m = c \cdot \frac{1}{(1 - \epsilon^2)^{\frac{3}{2}}} \quad (15)$$

In sum, the squeeze-film air damping force for this e-VEH device with no stoppers on the bottom plate could be calculated as:

$$F_{air} = -c \cdot v - K \cdot (h_0 - h) \\ = \begin{cases} c = \frac{\mu(2l)^4}{h_0^3} \cdot 0.42 \cdot \left(1 + \chi \frac{6\Lambda}{h_0} \right)^{-1} & K = 0 \quad (\sigma < 1) \\ \left\{ 1 + 3\eta \left(\frac{h_0}{l} \right) + 3\zeta \left(\frac{h_0}{l} \right)^2 \right\} \\ c_m = c \cdot \frac{1}{(1 - \epsilon^2)^{\frac{3}{2}}} & K = \frac{AP_0\sigma^2 b_1}{h_0} \cdot \frac{1 + 3\epsilon^2 + \frac{3}{8}\epsilon^4}{(1 - \epsilon^2)^{\frac{9}{2}}} \end{cases} \quad (16)$$

(other)

Whereas, the effect of the stoppers on the bottom plate to the air damping force also need to be considered. Thus, we have used finite element modeling method (COMSOL) to study the influence. In this COMSOL model, the meshes for the silicon beams and proof mass were set individually according to the critical dimensions. The meshing for the proof mass are set as "fine" calibrated with general physics, while the four silicon beams are meshed as "normal" calibrated with general physics, both with free tetrahedral elements. During the work, we have tried to tune the meshing condition with finer elements but no significant change has been observed for the simulation results, which indicates the accurate meshing condition. The results for the pressure caused by air damping force are shown in Fig. 4. Fig. 4(a) shows a device with gap of $220 \mu\text{m}$ and stopper height of $40 \mu\text{m}$, and Fig. 4(b) shows a device with gap of $220 \mu\text{m}$ but no stoppers. They were simulated at the same displacement and velocity during vibration. It can be noticed that, the stoppers not only influence the distribution of the air damping force, but also increase the overall damping remarkably. To study this influence in detail, we have divided the area of the bottom plate into two parts, which are the bottom surface and the stopper surface. The air damping forces are calculated for each part individually and then summed up:

$$F_{air} = F_{bottom} + F_{stopper} \quad (17)$$

Besides, we believe that the stoppers also increase the squeeze number, for the air flow above the stoppers may show compressibility earlier than the bottom surface. This means for devices with stoppers, the influence of finite squeeze number should be considered at gap larger than $60 \mu\text{m}$ according to the height of the stoppers.

2.2. Electrostatic force

As shown in Fig. 2, the induced charge, Q , on the top electrode (the bottom surface of the proof mass) can be calculated based on Kirchhoff's law and be simplified to:

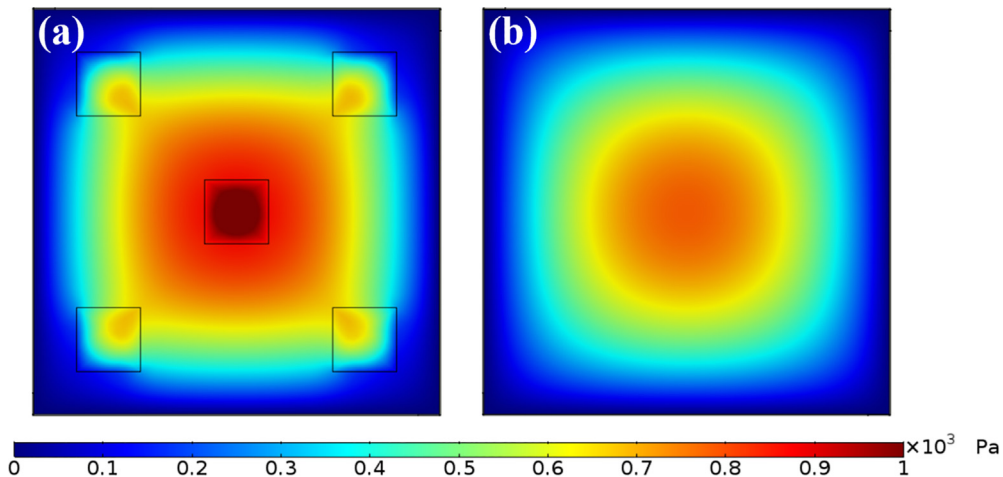


Fig. 4. The pressure of air damping for bottom plates with (a) $220 \mu\text{m}$ gap and $40 \mu\text{m}$ stoppers; (b) $220 \mu\text{m}$ gap and no stoppers.

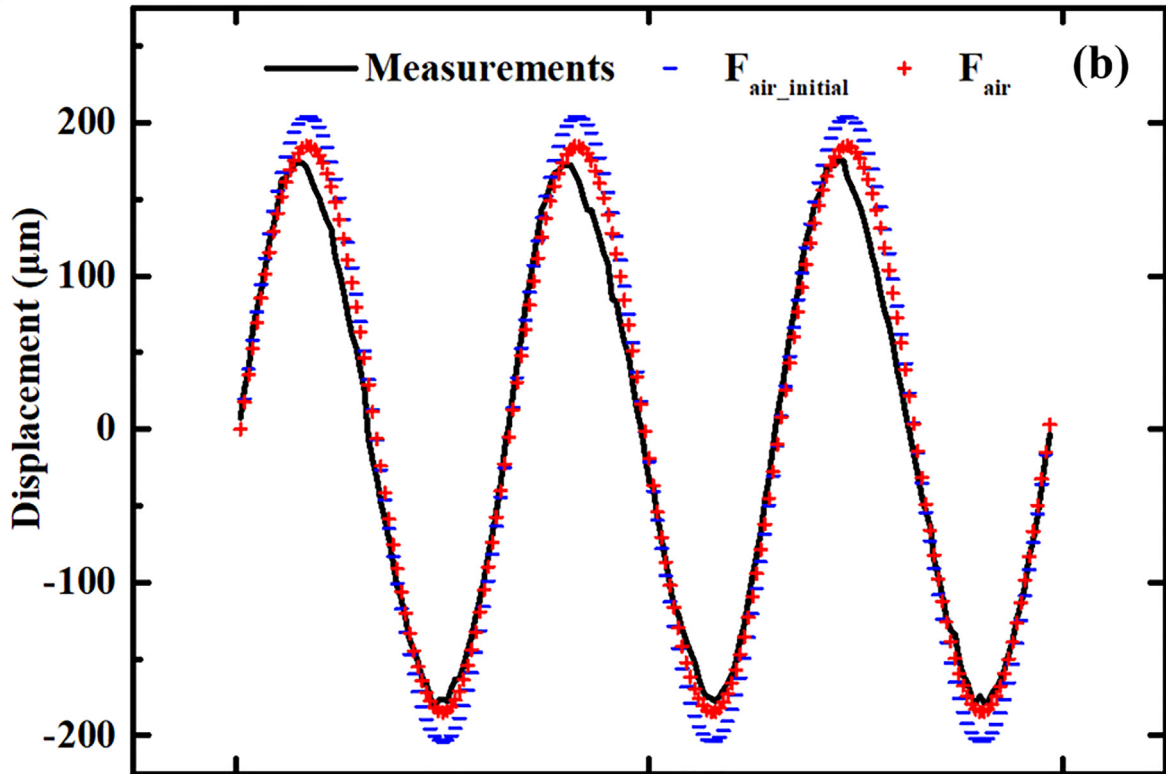
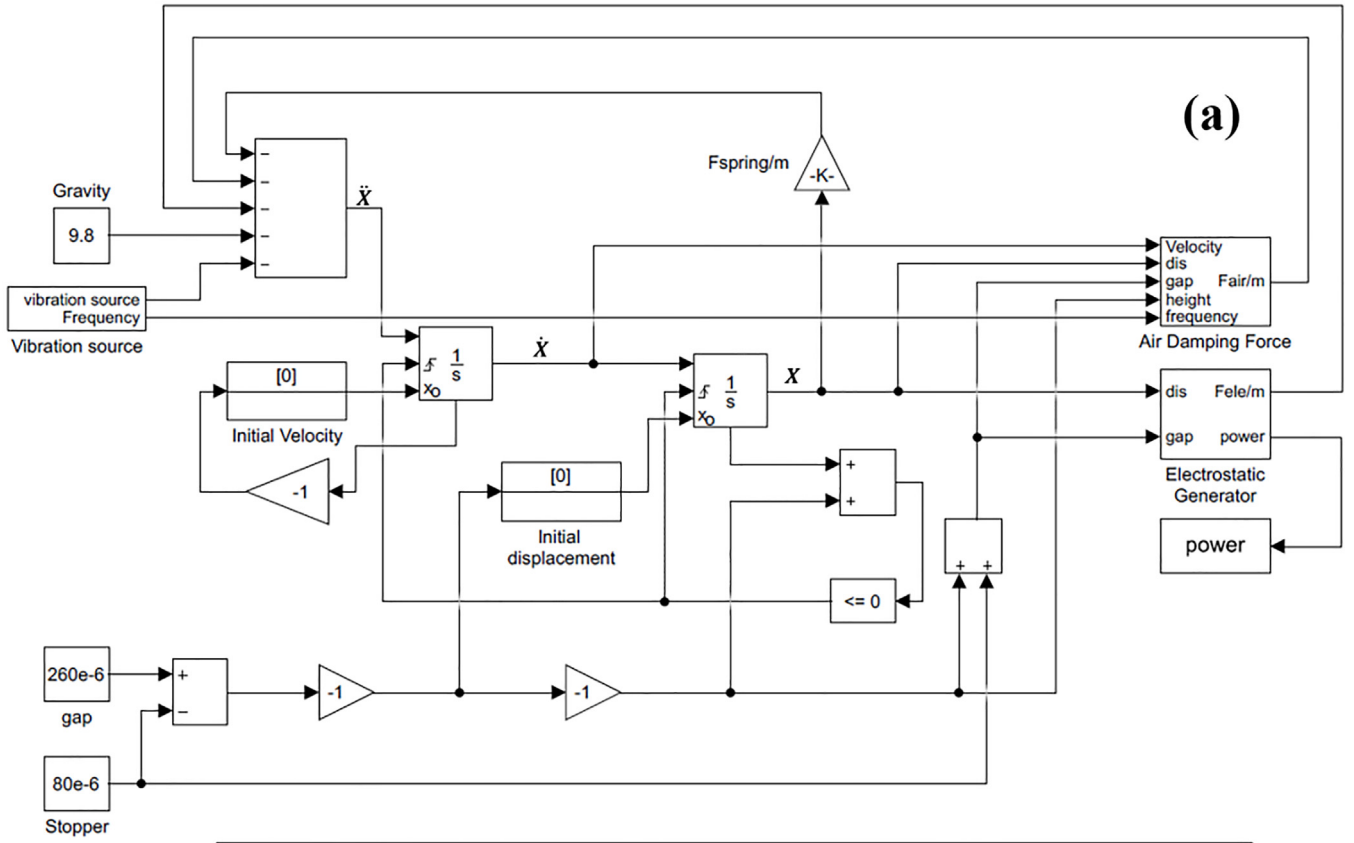


Fig. 5. (a) The Simulink model of the e-VEH; (b) the comparison between the measurements and simulation results for a device with 220 μm gap and without stoppers and surface potential.

$$Q = \int \left[\left(\frac{V_s}{R} - \frac{Q}{RC(t)} \right) \left(1 + \frac{2C_{par}}{C(t)} \right) \right] dt \quad (18)$$

capacitance formed by the capacitance of the air gap, $C_{air}(t)$, and the capacitance of the electret, C_{ele} . And the $C(t)$ is calculated as,

This total capacitance $C(t)$, corresponds to the serial linked

Table 1
Parameters of the simulation.

Symbol	Value
h	200, 220, 260, 300 μm
h_s	20, 40, 60, 80 μm
V_s	-350, -450, -600 V
m	0.1 g
d_{ele}	10 μm
f_0	135 Hz
C_{par}	50pf

$$\frac{1}{C(t)} = \frac{1}{C_{air}(t)} + \frac{1}{C_{ele}} \quad (19)$$

Thus, the electrostatic energy stored in this capacitance is:

$$E = \frac{Q^2}{2C(t)} \quad (20)$$

And the electrostatic force can be calculated as:

$$F_{ele} = \left| \frac{\partial E}{\partial x} \right| = \frac{Q^2}{2\epsilon A} \quad (21)$$

A. Simulink model

Based on the equations discussed above, Simulink Model has been made as shown in Fig. 5(a). Fig. 5(b) shows the comparison between the measurements and the simulation results for a device with gap of 220 μm while without stoppers or surface potential. The minus sign stands for the results obtained through the initial air damping equation without modifications, which is the Eq. (8). The plus sign stands for the simulation results after modifications discussed above. The error of the maximum and minimum displacement of the simulation compared to the experiments is 4% for the modified air damping model while it is 17% for the original air damping model. It can be noticed that the modified equation is more accurate and can reveal the displacement of the proof mass.

Some parameters in the Simulink model are set with the value shown in Table 1. From our previous work, when the vibration amplitude of the proof mass is larger than the initial gap, an additional collision force should be added to the model [35] or the velocity of the proof mass should be tuned [32] after collision. In this model, we considered the impact as perfect elastic collision which would tune the velocity of the mass when collision happens. An estimated capacitor of 50 pF has been included in the model to reflect the parasitic effect from the practical circuit.

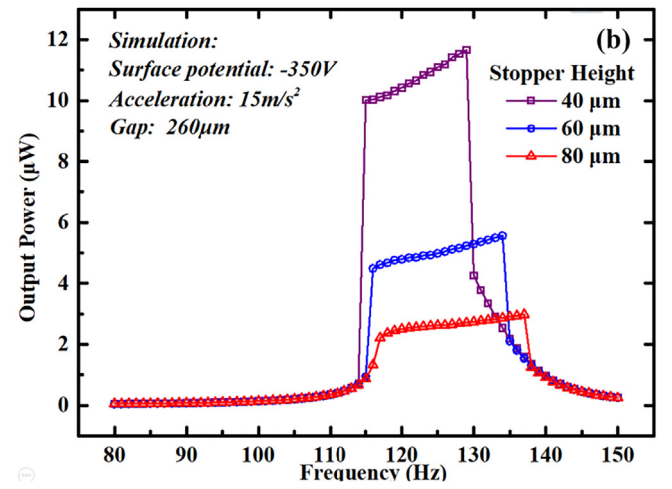
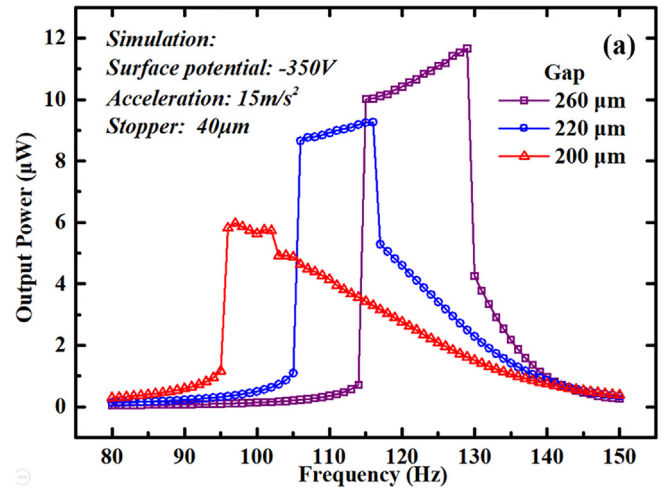


Fig. 7. Simulation results for devices with (a) various gaps and (b) various stopper heights.

2.3. Simulation

2.3.1. Surface potential

Simulation was performed by this Simulink model to explore the influence of surface potential, gap and stopper height to the device performance. Firstly, we have calculated the root mean square (RMS) output power of a harvester with various surface potentials at the same acceleration of 7 m/s^2 , as shown in Fig. 6(a). For all the surface potentials, same gap of 260 μm , and stopper height of 80 μm were defined

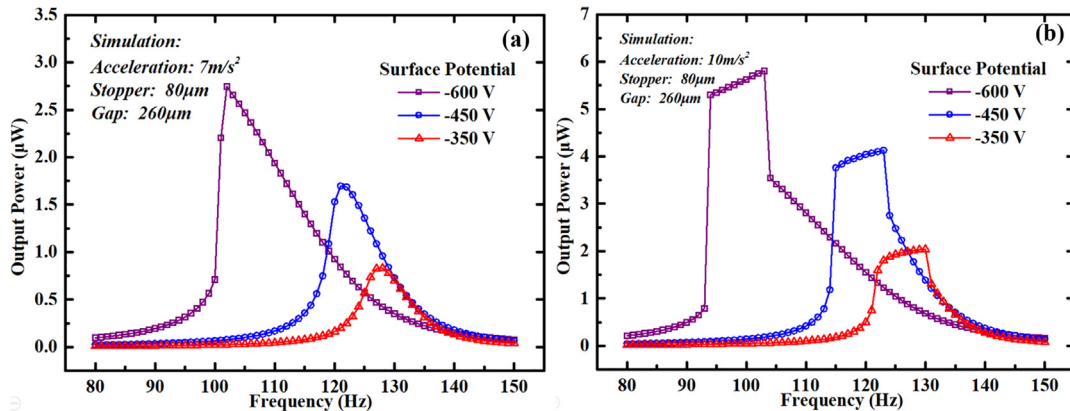


Fig. 6. Simulation results for a device under various surface potentials (a) with no collision; (b) with collision.

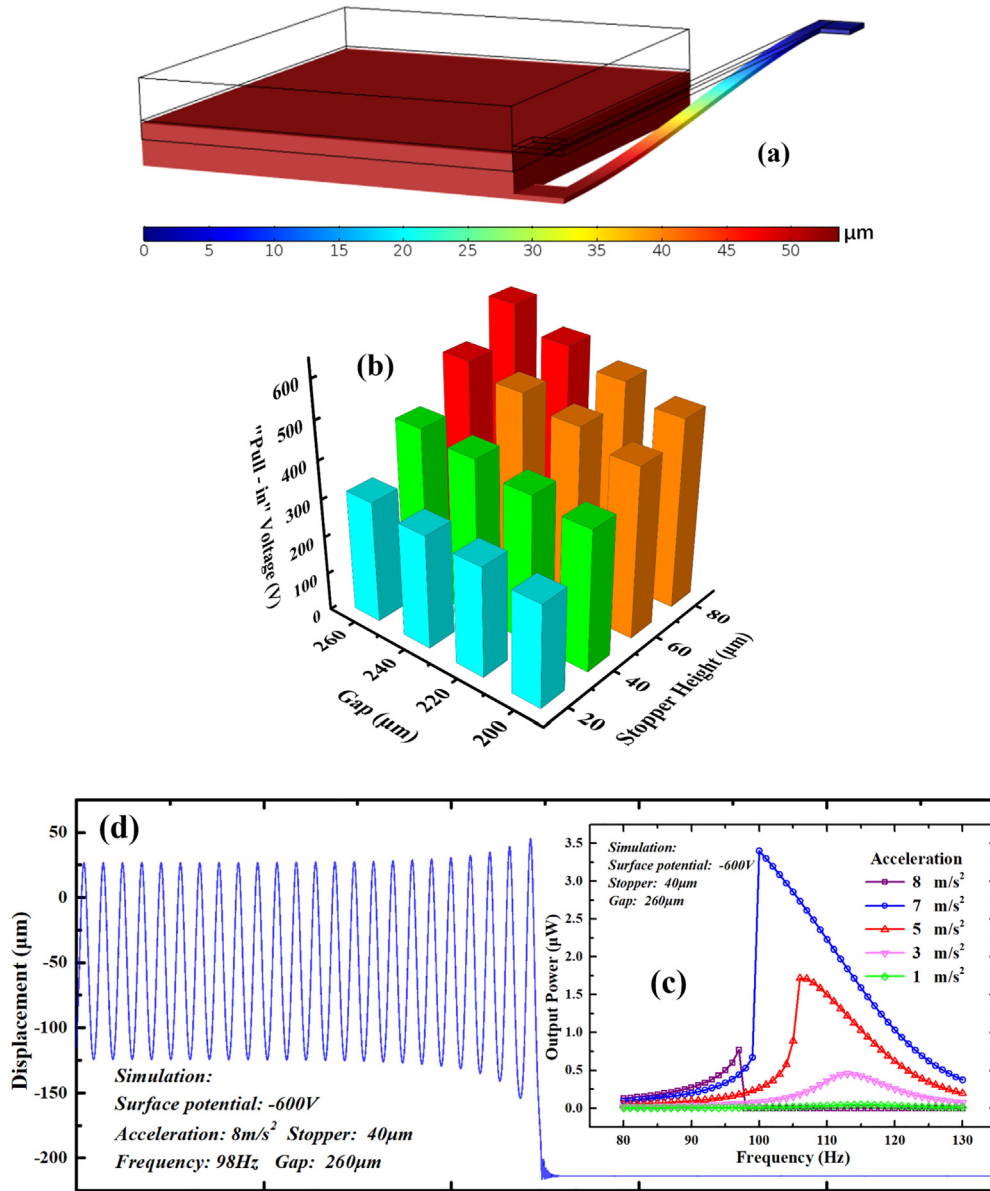


Fig. 8. (a) The COMSOL model; (b) Simulation results of the “pull-in” voltage for devices with various stopper heights and gaps; (c) Simulation results of the RMS output power versus frequency for a device with increasing acceleration; (d) Simulation results of the displacement of the device at 8 m/s² and 98 Hz.

in the model. A decrease of the resonant frequency and an increase of the output power have been noticed with the increased surface potential. This is due to the fact that the large surface potential induces more charges, which would lead to a large electrostatic force. A higher acceleration of 10 m/s² has also been applied to study the mechanical collision between the proof mass and the bottom plate. As shown in Fig. 6(b), a similar shift of resonant frequency and a broad bandwidth of the device can be observed. It can also be noticed that the bandwidth of Fig. 6(b) is wider than that of Fig. 6(a). With large acceleration, collision occurs between the proof mass and the stopper; therefore, the maximum displacement of the proof mass will be strictly limited and thus also the output voltage. Under this circumstance, the energy that can be harvested for each vibration circle is constant and the output power is linearly proportional to the vibration frequency.

2.3.2. Gap & stopper height

Both the air gap and the stopper height would affect the mechanical performance of the harvester. Fig. 7(a) shows the simulation for the harvester with air gap of 200, 220, and 260 μm, respectively. With a

large gap, the maximum variation range of the capacitance is large; therefore, the maximum power output could be improved. Furthermore, the resonant frequency would increase with the increased gap due to the decreased electrostatic force. Fig. 7(b) shows the effect of stopper height on the output power for devices with the same surface potential (-350 V) and the same gap (260 μm). Since the stopper height defines the maximum capacitance between the proof mass and the bottom electrode, larger RMS output power could be harvested when the stopper height decreases from 80 μm to 40 μm.

2.3.3. Pull-in effect

Although a decrease of the stopper height or an increase of the surface potential can significantly increase the maximum output power, they might also lead to the “pull-in” effect. Generally, the “pull-in” voltage for a static device is defined as:

$$V_p = \sqrt{\frac{8kh}{27A\epsilon\epsilon_0}} \quad (22)$$

We have studied the “pull-in” effect with COMSOL simulation

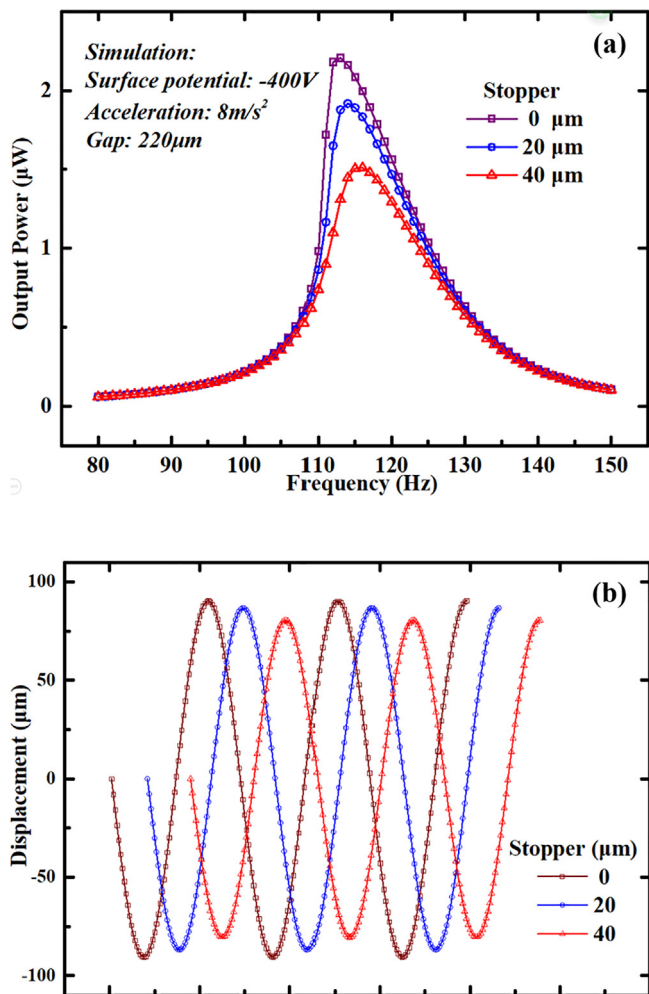


Fig. 9. Simulation results for devices with various stopper heights. (a) Output power versus frequency; (b) displacement at maximum output power.

Table 2
Parameters of the Device.

Symbol	Value
l	8 mm
w	200 μm
t	60 μm
m	0.1 g
H	500 μm
h_0	220, 260, 300 μm
h_s	0, 20, 40, 60, 80 μm
d	10 μm
V_s	-350, -400, -450, -600 V

through the electromechanical coupling. Thanks to the symmetry of the geometry, the simulation was performed with a quarter of the device. When 220 μm gap and no stoppers under the -550 V surface potential was applied, and the simulated displacement was shown in Fig. 8(a). In this stationary COMSOL model, when the plate position is lower than one-third of the gap between the two electrodes, “pull-in” effect would occur and the critical “pull-in” voltage could be obtained for different devices. Whereas, during the vibration of the energy harvester, the generated current will reduce the surface potential and the electrostatic force; therefore, the “pull-in” voltage is more complicated than stationary case, which will vary with the vibration amplitude and frequency. The Simulink model was applied for a parametric study of the dynamic “pull-in” voltages with various gaps and stopper heights, as

shown in Fig. 8(b).

For a device with stopper gap of 260 μm, height of 40 μm and surface potential of -600 V, its output power keeps increasing with increased acceleration as shown in Fig. 8(c). When the acceleration reaches to 8 m/s², however, the proof mass was pulled to the bottom electrode by the extremely large electrostatic force. As shown in Fig. 8(d), the device stopped vibrating due to the “pull-in” effect and no energy could be harvested afterwards.

2.3.4. Air damping

As shown in Fig. 4, the stopper structure could not only limit the maximum displacement of the mass to avoid the “pull-in” effect, but also changes the air damping when the proof mass is vibrating close to the bottom electrode. Fig. 9(a) shows the output power of the harvesters with the same gap but various stopper heights when a low acceleration of 8 m/s² was applied. Although none of the harvesters encounter collision, we have still noticed a slight difference of the output power. This is mainly due to the fact that air damping is more significant for the device with higher stoppers which are closer to the proof mass under the same vibration source. This is confirmed by the simulated displacement of these devices as shown in Fig. 9(b). It should also be noticed that the softening effect of electrostatic force is more significant than the effect of air damping force during this simulation; therefore, the resonant frequency of the harvester decreases with the decreased stopper height.

3. Device fabrication

We have designed and fabricated the e-VEHs with the parameters listed in Table 2. Silicon wafers were used as the main material for our devices. A 10 μm CYTOP layer was used as the electret material on the bottom plate and a metal layer of 15 nm Cr and 100 nm Au was used as electrode. Fig. 10(a) shows the fabrication processes for the bottom electrode in cavity, which is described as below:

- Step 1. Silicon wafer with 500 μm thickness and 2 μm oxide layers on both sides was obtained by thermally oxidized.
- Step 2–4. Lithography was applied on the top side of the wafer. Then the top side was etched with buffer oxide etchant (BOE) with another side protected by pre-coated photoresist. After these two steps, the wafer was etched in 40% KOH at 50°C to get stoppers with specific height.
- Step 5–6. ICP-RIE was applied to etch SiO₂ on stoppers. Then the KOH solution was applied again to form the cavity with the depth we designed, which is used for controlling the initial gap. And BOE was applied to etch all the SiO₂ remained.
- Step 7–8. A metal layer of Cr (15 nm)-Al (100 nm) as electrode was deposited by sputtering on the bottom side of the wafer. And 10 μm CYTOP layer as electret was spray coated on the top of the plate.

The process flow for the mass suspended by four silicon beams is shown in Fig. 10(b):

- Step 1. Silicon wafer with 500 μm thickness and 2 μm oxide layers on both sides was obtained by thermally oxidized.
- Step 2–4. Lithography was applied on the top side of the wafer. Then the top side was etched with BOE with another side protected by pre-coated photoresist. After these two steps, the wafer was etched in 40% KOH at 50°C to get a cavity with 280 μm depth.
- Step 5–6. Lithography was further applied to the bottom surface then the patterned SiO₂ was dry etched with ICP-RIE process. And after these two steps, the remained photoresist was removed.
- Step 7. The KOH solution was applied again to release the silicon beams. And BOE was applied to etch all the SiO₂ remained.
- Step 8. A metal layer of Cr (15 nm)-Al (100 nm) as electrode was deposited by sputtering on the bottom side of the wafer.

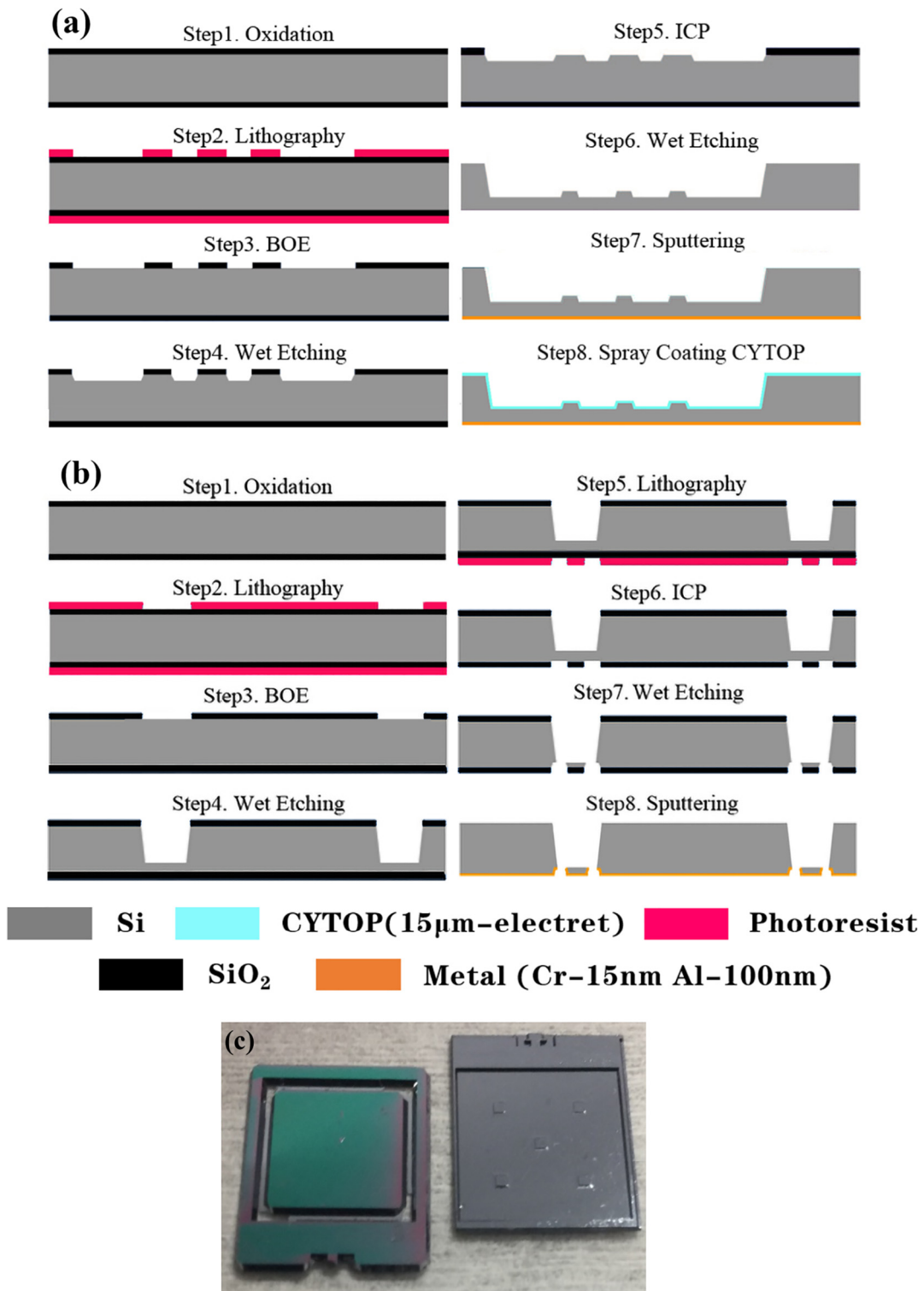


Fig. 10. The fabrication process for (a) the bottom plate; (b) the proof mass; (c) the top and bottom plates before assembling.

Fig. 10(c) shows the fabricated proof mass (left) and the bottom electrode (right), respectively. The two components have an overall size of 1.1 cm × 1.3 cm, which are manually assembled for the following tests.

4. Characterization

As shown in Fig. 11, the final e-VEH device was mounted on a shaker with a reference accelerometer to monitor and control the

vibration amplitude during the test. A laser detector was used to measure the displacement of the proof mass during vibration.

4.1. Surface potential

Fig. 12 shows the measurements of harvested RMS power versus frequency under different conditions. It could be noticed that these figures show similar results to the simulation results as discussed above. With higher surface potential, both an increase of the output power and

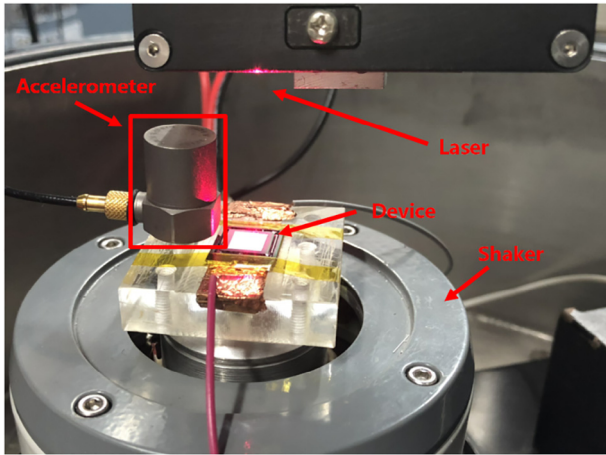


Fig. 11. The device is fixed on a stage and tested on a shaker with an accelerometer and a laser was used to monitor the displacement of the proof mass during vibration.

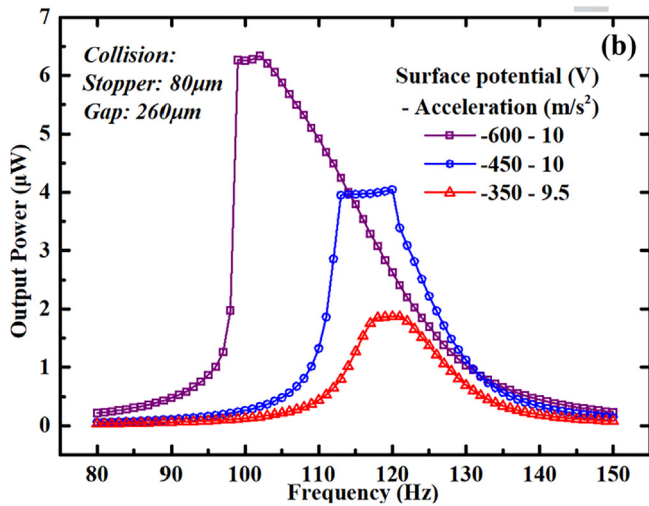
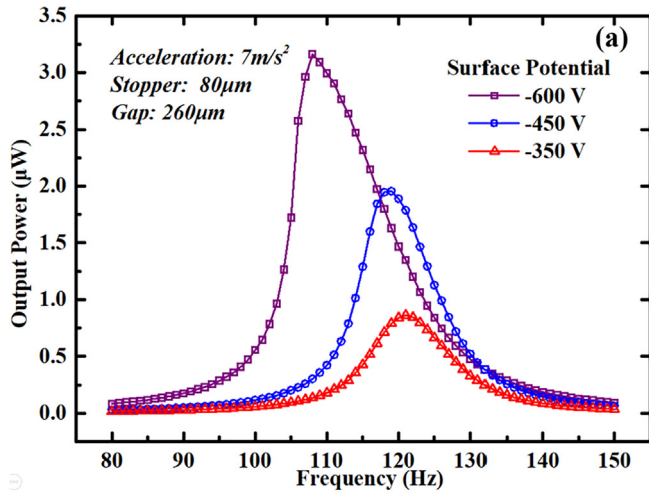


Fig. 12. The measured RMS output power versus frequency for a device with various surface potentials.

a decrease of the resonant frequency have been noticed as shown in Fig. 12(a). The harvesters have achieved the maximum output power when the proof mass collided with the bottom plate. It should be noted

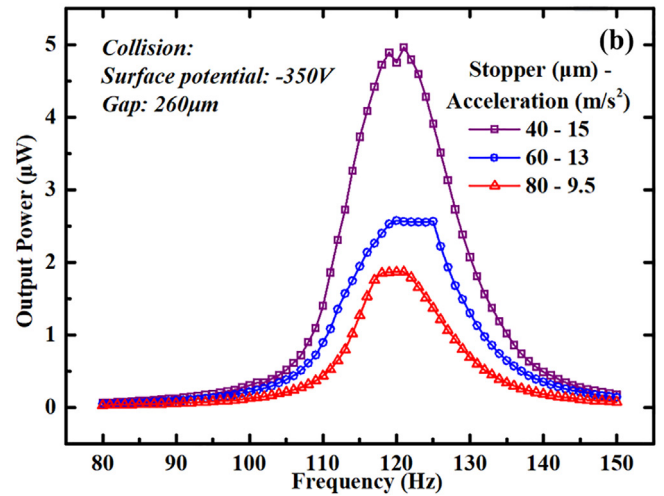
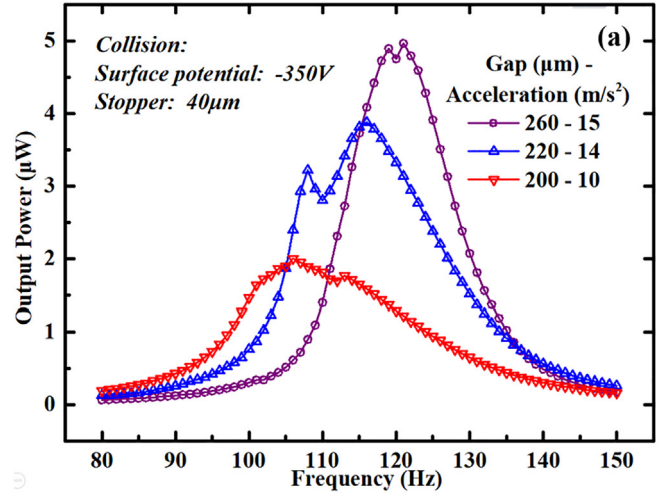


Fig. 13. The measured RMS output power versus frequency for devices with various (a) gaps and (b) stopper heights.

that, when collision happens, the downward displacement of proof mass is mainly dependent on the gap and stopper height, which saturates to a certain level according to the device geometry. Further increasing the acceleration only leads to a broader bandwidth without improving the output power significantly [43]. On the other hand, high acceleration might induce unstable vibration, which might cause a decrease of the RMS output power or damage of the device [44]. During this test, therefore, we controlled the acceleration in a range that the proof mass is just colliding with the bottom plate.

4.2. Gap & stopper height

Fig. 13 shows the measurements for devices with various stopper heights and gaps at the same surface potential when mechanical collision occurs. According to the theoretical analysis and Simulink modeling above, the output power is dependent on the capacitance change of the device during vibration. With a fixed stopper height of $40\mu\text{m}$, as shown in Fig. 13(a), larger gap distance gives higher output power since the minimum capacitance is decreased. On the other hand, higher power could be harvested from lower stoppers thanks to the larger maximum capacitance when the proof mass collides with the bottom electrode, as shown in Fig. 13(b). These experiments agree well with the simulation results in Fig. 7. It should be noted that the bandwidth of 260-15 curve seems not wider than that of 220-14 curve even a higher acceleration amplitude is applied, as shown in Fig. 13a. This is mainly due to the instability and turbulence of the vibration (for both two

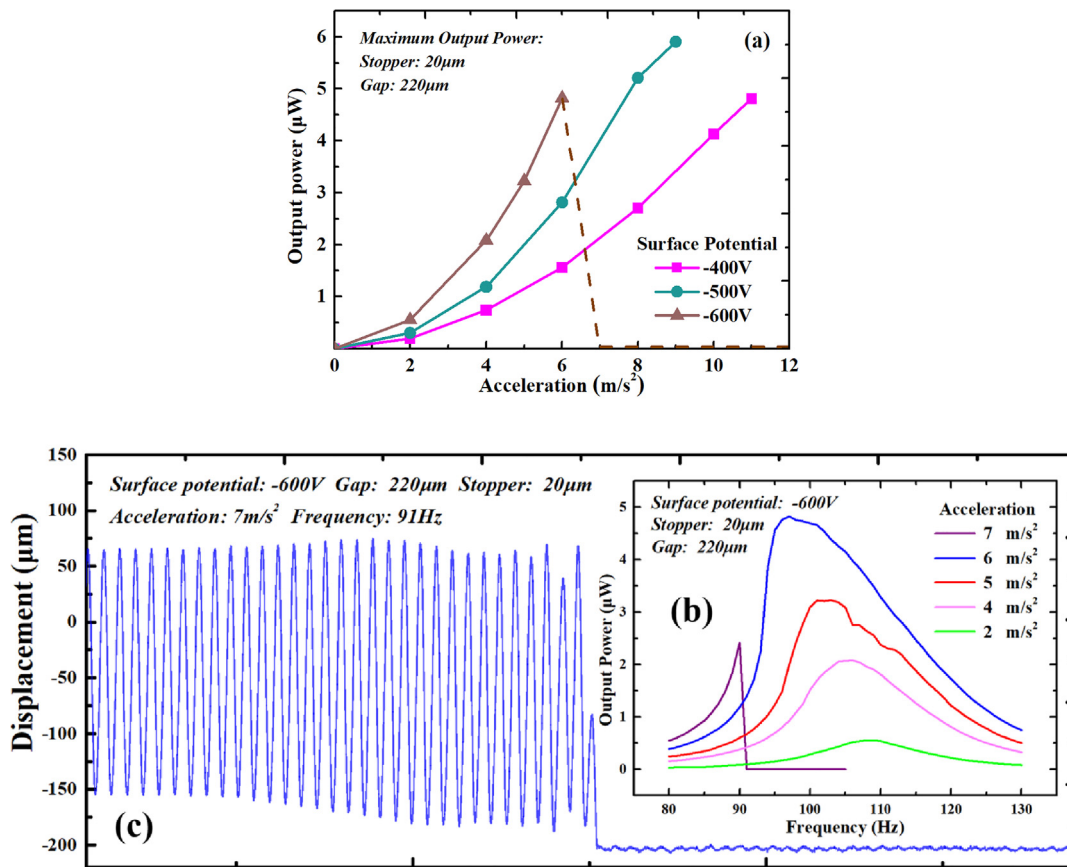


Fig. 14. (a) The maximum output power versus acceleration for a device with various surface potentials; (b) measurements for the device with surface potential of -600 V at various accelerations; (c) the measured displacement of the device at 7 m/s^2 and 91 Hz when “pull-in” happened.

cases) when mechanical collision occurs during the experiment.

4.3. “Pull-in” effect

To study the “pull-in” effect of our electrostatic harvester, we have gradually increased the acceleration of vibration source for the devices with surface potential from -400 V to -600 V . Fig. 14(a) shows the measurements of the output power for a device with gap of $220 \mu\text{m}$ and stopper height of $20 \mu\text{m}$. The output of the device usually increases when the acceleration gradually increases up to 11 m/s^2 . However, the device with surface potential of -600 V induced the “pull-in” effect during the test, when an acceleration of 7 m/s^2 was applied. Fig. 14(b) shows the frequency spectrum measurements of the output power at various accelerations. It could be noticed that the “pull-in” effect happened at 7 m/s^2 and 91 Hz . Fig. 14(c) shows the displacement of the device at this condition. The proof mass has been pulled to the bottom plate; therefore, the whole device was unable to harvest vibrational energy anymore. To our best knowledge, this is for the first time to observe the “pull-in” effect of an energy harvester during vibration, which provides interesting information on the optimal design of the device.

4.4. Air damping

Fig. 15(a) shows the effect of the stopper height and the vibration amplitude on the output of the devices with the same gap of $220 \mu\text{m}$ and surface potential of -400 V . It should be noted that the device could harvest more power with lower stopper height (or no stopper), though no collision occurs under a low acceleration of vibration source. This phenomenon reflects the effect of air damping difference among the three devices. Fig. 15(b) shows their displacement at 6 m/s^2 at their

resonant frequency, which is 120 Hz , 118 Hz , and 119 Hz , for devices with stopper height of $0 \mu\text{m}$, $20 \mu\text{m}$, and $40 \mu\text{m}$, respectively. It could be noticed that devices with lower stopper height exhibit a larger vibration amplitude, which agrees well with the simulation above. This is mainly due to the fact that higher stopper induces larger air damping force which limits the vibration of the proof mass.

5. Discussion

Based on the simulation and the measurements of the e-VEH devices, we noticed that some important factors must be considered and balanced to optimize the power output of the harvester with out-of-plane gap-closing scheme.

5.1. Surface potential

It is commonly known that higher surface potential leads to higher output power both in small and large accelerations. This could be explained by two aspects: 1. Higher surface potential means more charges could be induced. 2. Higher surface potential leads to a lower balance location for large downward electrostatic force, at which the same vibration amplitude would cause larger capacitance variation. Besides, higher surface potential will also lead to a lower resonant frequency. With high surface potential (-600 V in our work), however, both the simulation and the experiments have demonstrated a high risk of the “pull-in” effect.

5.2. Gap, and stopper height

When the external excitation is large enough to make the proof mass collide with the bottom plate, the stopper will limit the maximum

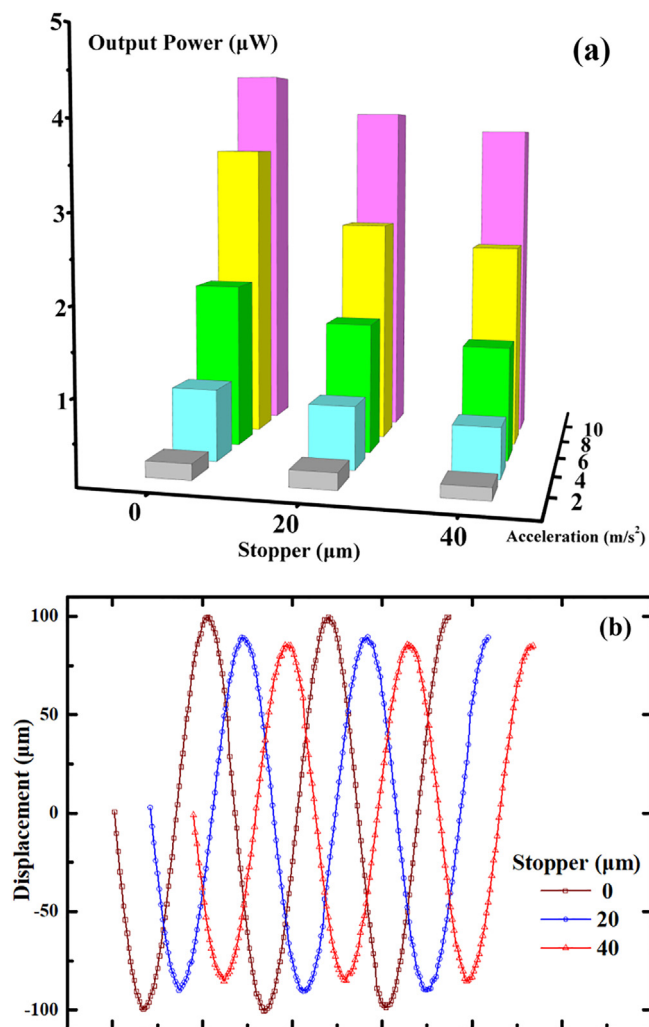


Fig. 15. (a) Measured maximum output power for devices with various stopper heights at various accelerations; (b) displacement for devices at 6 m/s^2 and their resonant frequencies.

vibration amplitude of the proof mass. On one hand, this limitation could protect the device from the “pull-in” effect of high surface potential. Furthermore, the mechanical collision would increase the bandwidth of the harvester, which means the device could harvest energy from a broad frequency range of vibration sources. On the other hand, the minimum and maximum capacitance of the harvester depend on the gap distance and the stopper height; therefore, small gap or high stopper would also limit the maximum power output of the device.

5.3. “Pull-in” effect

“Pull-in” effect must be considered and avoided to optimize the design of device since it may lead to the failure of e-VEHs. Generally, there are three aspects to avoid this effect for our device. Firstly, we can increase the stopper height to limit the minimum gap distance between the proof mass and the bottom electrode, which determines the maximum electrostatic force. Secondly, we could increase the initial gap which increases the maximum spring force from the beam structure. Thirdly, the electrostatic force could also be decreased if we limit the surface potential of the electret layer. As discussed above, however, all these methods will cause the decrease of the output power. Therefore, all these parameters should be well balanced to optimize the device output performance. Our theoretical analysis and simulation provide a promising route for the optimization of the vibration energy harvester.

6. Conclusion

In this paper, a comprehensive model including the nonlinear air damping force and the “pull-in” effect of electrostatic force is presented for the optimization of e-VEHs. The simulation results are in excellent agreement with the measurements. From this model, we can easily explore the influence of the stopper height and gap on the device performance. As expected, the “pull-in” phenomenon has been observed during the energy harvesting process for the first time. A few regulations concluded in this study regarding to the height of stopper, the surface potential and the initial air gap can provide useful information for the optimal design of the e-VEH device. We shall balance the gap and stopper height to achieve low air damping force and high output power while avoiding the “pull-in” effect.

Declaration of Competing Interest

The authors declare that they have no known competing financial interests or personal relationships that could have appeared to influence the work reported in this paper.

Acknowledgments

We would like to acknowledge the technical support from the Materials Characterization and Preparation Center, Southern University of Science and Technology. This work was supported in part by the Shenzhen Science and Technology Innovation Committee under Grants JCYJ20170412154426330, in part by the Guangdong Natural Science Funds under Grants 2016A030306042 and 2018A050506001.

References

- [1] Ulukus S, Yener A, Erkip E, Simeone O, Zorzi M, Grover P, et al. Energy harvesting wireless communications: a review of recent advances. *IEEE J Sel Areas Commun* 2015;33:360–81. <https://doi.org/10.1109/JSAC.2015.2391531>.
- [2] Jr BEW. Beyond the battery. *Nat Nanotechnol* 2008;3:71–2.
- [3] Kamalinejad P, Mahapatra C, Sheng Z, Mirabbasi S, Victor VC, Guan YL. Wireless energy harvesting for the internet of Things. *IEEE Commun Mag* 2015;53:102–8. <https://doi.org/10.1109/MCOM.2015.7120024>.
- [4] Suzuki Y. Recent progress in MEMS electret generator for energy harvesting. *IEEJ Trans Electr Electron Eng* 2011;6:101–11. <https://doi.org/10.1002/tee.20631>.
- [5] Crovetto A, Wang F, Hansen O. An electret-based energy harvesting device with a wafer-level fabrication process. *J Micromech Microeng* 2013;23:114010. <https://doi.org/10.1088/0960-1317/23/11/114010>.
- [6] Wu Y, Hu Y, Huang Z, Lee C, Wang F. Electret-material enhanced triboelectric energy harvesting from air flow for self-powered wireless temperature sensor network. *Sensors Actuat A Phys* 2018;271:364–72. <https://doi.org/10.1016/j.sna.2017.12.067>.
- [7] Fan K, Chang J, Chao F, Pedrycz W. Design and development of a multipurpose piezoelectric energy harvester. *Energy Convers Manage* 2015;96:430–9. <https://doi.org/10.1016/j.enconman.2015.03.014>.
- [8] Cuadras A, Gasulla M, Ferrari V. Thermal energy harvesting through pyroelectricity. *Sensors Actuat A Phys* 2010;158:132–9. <https://doi.org/10.1016/j.sna.2009.12.018>.
- [9] Wu Y, Zhang H, Zuo L. Thermoelectric energy harvesting for the gas turbine sensing and monitoring system. *Energy Convers Manage* 2018;157:215–23. <https://doi.org/10.1016/j.enconman.2017.12.009>.
- [10] Shan X, Li H, Yang Y, Feng J, Wang Y, Xie T. Enhancing the performance of an underwater piezoelectric energy harvester based on flow-induced vibration. *Energy* 2019;172:134–40. <https://doi.org/10.1016/j.energy.2019.01.120>.
- [11] Wang J, Zhou S, Zhang Z, Yurchenko D. High-performance piezoelectric wind energy harvester with Y-shaped attachments. *Energy Convers Manage* 2019;181:645–52. <https://doi.org/10.1016/j.enconman.2018.12.034>.
- [12] Iqbal M, Khan FU. Hybrid vibration and wind energy harvesting using combined piezoelectric and electromagnetic conversion for bridge health monitoring applications. *Energy Convers Manage* 2018;172:611–8. <https://doi.org/10.1016/j.enconman.2018.07.044>.
- [13] Zhang Y, Hu Y, Guo X, Wang F. Micro energy harvester with dual electrets on sandwich structure optimized by air damping control for wireless sensor network application. *IEEE Access* 2018;6:26779–88. <https://doi.org/10.1109/ACCESS.2018.2836381>.
- [14] Zhang Y, Cao J, Zhu H, Lei Y. Design, modeling and experimental verification of circular Halbach electromagnetic energy harvesting from bearing motion. *Energy Convers Manage* 2019;180:811–21. <https://doi.org/10.1016/j.enconman.2018.11.037>.
- [15] Fan K, Cai M, Wang F, Tang L, Liang J, Wu Y, et al. A string-suspended and driven

- rotor for efficient ultra-low frequency mechanical energy harvesting. *Energy Convers Manage* 2019;198:111820 <https://doi.org/10.1016/j.enconman.2019.111820>.
- [16] Li Z, Yan Z, Luo J, Yang Z. Performance comparison of electromagnetic energy harvesters based on magnet arrays of alternating polarity and configuration. *Energy Convers Manage* 2019;179:132–40. <https://doi.org/10.1016/j.enconman.2018.10.060>.
- [17] Wu Y, Qiu J, Zhou S, Ji H, Chen Y, Li S. A piezoelectric spring pendulum oscillator used for multi-directional and ultra-low frequency vibration energy harvesting. *Appl Energy* 2018;231:600–14. <https://doi.org/10.1016/j.apenergy.2018.09.082>.
- [18] Li S, Crovetto A, Peng Z, Zhang A, Hansen O, Wang M, et al. Bi-resonant structure with piezoelectric PVDF films for energy harvesting from random vibration sources at low frequency. *Sensors Actuata A Phys* 2016;247:547–54. <https://doi.org/10.1016/j.sna.2016.06.033>.
- [19] Izadgoshab I, Lim YY, Tang L, Padilla RV, Tang ZS, Sedighi M. Improving efficiency of piezoelectric based energy harvesting from human motions using double pendulum system. *Energy Convers Manage* 2019;184:559–70. <https://doi.org/10.1016/j.enconman.2019.02.001>.
- [20] Suzuki Y, Miki D, Edamoto M, Honzumi M. A MEMS electret generator with electrostatic levitation for vibration-driven energy-harvesting applications. *J Micromech Microeng* 2010;20. <https://doi.org/10.1088/0960-1317/20/10/104002>.
- [21] Wang F, Hansen O. Electrostatic energy harvesting device with out-of-the-plane gap closing scheme. *Sens Actuata A Phys* 2014;211:131–7. <https://doi.org/10.1016/j.sna.2014.02.027>.
- [22] Tao K, Lye SW, Miao J, Tang L, Hu X. Out-of-plane electret-based MEMS energy harvester with the combined nonlinear effect from electrostatic force and a mechanical elastic stopper. *J Micromech Microeng* 2015;25. <https://doi.org/10.1088/0960-1317/25/10/104014>.
- [23] Xu Y, Luo A, Zhang A, Zhang Y, Tang B, Wang K, et al. Spray coating of polymer electret with polystyrene nanoparticles for electrostatic energy harvesting. *Micro Nano Lett* 2016;11:640–4. <https://doi.org/10.1049/mnl.2016.0336>.
- [24] Honma H, Mitsuya H, Hashiguchi G, Fujita H, Toshiyoshi H. Improvement of energy conversion effectiveness and maximum output power of electrostatic induction-type MEMS energy harvesters by using symmetric comb-electrode structures. *J Micromech Microeng* 2018;28. <https://doi.org/10.1088/1361-6439/aab514>.
- [25] Chiu Y, Lee YC. Flat and robust out-of-plane vibrational electret energy harvester. *J Micromech Microeng* 2013;23. <https://doi.org/10.1088/0960-1317/23/1/015012>.
- [26] Boisseau S, Despesse G, Ricart T, Defay E, Sylvestre A. Cantilever-based electret energy harvesters. *Smart Mater Struct* 2011;20. <https://doi.org/10.1088/0964-1726/20/10/105013>.
- [27] Lu Y, Cottone F, Boisseau S, Marty F, Galayko D, Basset P. A nonlinear MEMS electrostatic kinetic energy harvester for human-powered biomedical devices. *Appl Phys Lett* 2015;107:20–4. <https://doi.org/10.1063/1.4937587>.
- [28] Harne RL, Wang KW. A review of the recent research on vibration energy harvesting via bistable systems. *Smart Mater Struct* 2013;22:023001 <https://doi.org/10.1088/0964-1726/22/2/023001>.
- [29] Zhou S, Cao J, Inman DJ, Lin J, Liu S, Wang Z. Broadband tristable energy harvester: modeling and experiment verification. *Appl Energy* 2014;133:33–9. <https://doi.org/10.1016/j.apenergy.2014.07.077>.
- [30] Zou Hong-Xiang, Zhang Wen-ming, Li Wen-Bo, Wei Ke-Xiang, Gao Qiu-Hua, Peng Zhi-Ke, Meng Guang. Design and experimental investigation of a magnetically coupled vibration energy harvester using two inverted piezoelectric cantilever beams for rotational motion. *Energy Convers Manage* 2017;148:1391–8. <https://doi.org/10.1016/j.enconman.2017.07.005>.
- [31] Mei X, Zhou S, Yang Z, Kaizuka T, Nakano K. The benefits of an asymmetric tristable energy harvester in low-frequency rotational motion. *Appl Phys Express* 2019;12:057002 <https://doi.org/10.7567/1882-0786/ab0b75>.
- [32] Li S, Peng Z, Zhang A, Luo D, Wang F. Dual resonant structure for energy harvesting from random vibration sources. 2016 IEEE 11th Annu Int Conf Nano/Micro Eng Mol Syst NEMS 2016 2016;015019:255–9. doi:10.1109/NEMS.2016.7758245.
- [33] Erturk A, Inman DJ. Broadband piezoelectric power generation on high-energy orbits of the bistable Duffing oscillator with electromechanical coupling. *J Sound Vib* 2011;330:2339–53. <https://doi.org/10.1016/j.jsv.2010.11.018>.
- [34] Murotani K, Suzuki YM. Electret energy harvester with embedded bistable electrostatic spring for broadband response. *J Micromech Microeng* 2018;28. <https://doi.org/10.1088/1361-6439/aac8cc>.
- [35] Zhang Y, Wang T, Zhang A, Peng Z, Luo D, Chen R, et al. Electrostatic energy harvesting device with dual resonant structure for wideband random vibration sources at low frequency. *Rev Sci Instrum* 2016;87. <https://doi.org/10.1063/1.4968811>.
- [36] Zhang Y, Wang T, Luo A, Hu Y, Li X, Wang F. Micro electrostatic energy harvester with both broad bandwidth and high normalized power density. *Appl Energy* 2018;212:362–71. <https://doi.org/10.1016/j.apenergy.2017.12.053>.
- [37] Bao M. *Analysis and design principles of MEMS devices*. Elsevier B.V. 2005.
- [38] Zhang WM, Yan H, Peng ZK, Meng G. Electrostatic pull-in instability in MEMS/NEMS: a review. *Sensors Actuata A Phys* 2014;214:187–218. <https://doi.org/10.1016/j.sna.2014.04.025>.
- [39] Zhang Y, Guo X, Liu Z, Luo A, Wang F. Two mechanical tuning schemes to improve the bandwidth of electret-based electrostatic energy harvester. *IEEE/ASME Int Conf Adv Intell Mechatronics, AIM* 2018;2018–July:375–80. doi: 10.1109/AIM.2018.8452233.
- [40] Compressible Salbu E, Films Squeeze, Bearings Squeeze. *J Basic Eng* 1964;355–64.
- [41] Gallis MA, Torczynski JR. An improved Reynolds-equation model for gas damping of microbeam motion. *J Microelectromech Syst* 2004;13:653–9. <https://doi.org/10.1109/JMEMS.2004.832194>.
- [42] Sadd MH, Stiffler AK. Squeeze film dampers: amplitude effects at low squeeze numbers. *Trans ASME* 1975;1366–70. <https://doi.org/10.1115/1.3438789>.
- [43] Zhang Y, Hu Y, Chen S, Peng Z, Li X, Wang F. Electret based micro energy harvesting device with both broad bandwidth and high power density from optimal air damping. *TRANSDUCERS 2017–19th Int Conf Solid-State Sensors, Actuat Microsyst* 2017:355–8. <https://doi.org/10.1109/TRANSDUCERS.2017.7994061>.
- [44] Guo X, Zhang Y, Wang F. Optimization of Electrostatic Energy Harvesting Device with Multi-Step Structure. *NEMS 2018 – 13th Annu IEEE Int Conf Nano/Micro Eng Mol Syst* 2018:167–172. doi:10.1109/NEMS.2018.8556985.